

Large Segmentation Design of Robust Photonic Quantum Gates

Khen Cohen, Haim Suchowski and Yaron Oz

School of Physics and Astronomy, Tel-Aviv University, Tel-Aviv 69978, Israel

(Dated: April 14, 2024)

We analyze the fidelity and power loss of photonic quantum gates, implemented by a segmentation of coupled optical waveguides, as functions of the number of segments. We show that designs with a large number of segments mitigate effectively the systematic errors for a wide range of error correlation strength and variance. We quantify the design roughness effect on the power loss and analyze the performance of various methods for smoothing the configuration of the waveguides. We observe an asymptotic scaling behaviour of the gate fidelity and power loss with the number of segments.

I. INTRODUCTION

The quest for harnessing the potential of quantum phenomena has been a driving force behind intensive fundamental research and technology efforts, including Quantum Information Processing (QIP) [1].

Quantum computers hold the promise for an exponential speedup in solving certain complex computational problems and a capability to decrypt classical encryption protocols in real-time, thereby opening new frontiers in computing and cryptography. Despite substantial theoretical advancements in quantum algorithms [2, 3], the practical realization of a quantum information processor remains a formidable challenge.

One of the paramount obstacles in achieving practical quantum computation lies in the noise and errors that affect the performance of the fundamental building blocks of quantum algorithms: the qubit's state preparation, the quantum gates, and the measurement process [4]. These errors and noise have various sources, such as fabrication imperfections [5], inaccurate coupling strengths and the interaction with the classical environment [6]. In response to these challenges, two primary routes have been taken: error-correcting codes [7] and error mitigation schemes [8, 9].

Error-correcting codes construct logical qubits using additional entangled physical qubits and can significantly outperform their physical counterparts. Notable among these codes are stabilizer codes, exemplified by the surface code [10], which exhibits a relative tolerance to local errors. Fault-tolerant quantum computation using error correcting codes requires the fidelity of the physical quantum gates to be above a certain threshold, making the reduction of the physical errors to be of utmost importance [11, 12].

Error mitigation schemes seek to reduce errors using sophisticated implementation and techniques, for a review see [8, 9]. One such framework is the segmented composite pulse design, which was originally used in atomic physics and nuclear magnetic resonance, employ-

ing a combination of constant pulses to minimize errors during the system evolution [13–16]. This error mitigation technique holds a promise for improving the performance of complex quantum algorithms, and has a broad applicability in diverse quantum computing realizations of quantum information processing devices.

In [17] smooth designs were proposed in a general composite pulses scheme, and [18] suggested symmetric and antisymmetric composite pulses with a large number of pulses in NMR. It has been recently shown in [19] that this method can be implemented in Silicon photonics [20] for designing robust high fidelity quantum gates by varying the waveguide geometry, and specifically its cross-section. The focus in [19] has been on having a small number of segments, under the assumption of fully correlated noise of the different waveguides. It was proven in [21] that there is a correlation strength threshold for the segmented design to be an effective error mitigating scheme.

The aim of the current work is to analyze the composite pulse scheme for optimizing robust designs with a large number of segments. We consider both the fidelity of the quantum gates as well as the power loss of the designs for varying systematic noise correlations. Applied to the photonic dual-rail realization, our methods yield robust high-fidelity unitary designs for single-qubit and hence also for the probabilistic double-qubit gates such as CZ and CNOT [22]. We consider different manufacturing configurations in Silicon and Lithium Niobate, as Silicon is widely used in this field, while the Lithium Niobate is considered to be a promising material for designing active QIPs.

Our main contributions are :

- 1. Enhanced Quantum Gate Robustness:** We demonstrate numerically that increasing the number of composite segments N results in a substantial improvement in the quantum gate mean fidelity $\mathbf{E}[F]$, and a reduction in its standard deviation $\sigma_F[F]$ with a certain scaling with N . We further

show that $N \sim O(10)$ is effective for most practical cases.

2. **Power Loss Analysis:** We quantify the impact of increasing N on the power loss in the quantum gate due to the back-scattering effects in the segments. We argue analytically and show numerically that the power loss grows linearly with the number of segments, which makes it necessary to apply smoothing methods to the large N designs.
3. **Correlation Strength:** We study the impact of error correlation strength between the different segments on the gate fidelity. We show that enhancing the correlation strength among the errors in different segments leads to a significant increase in the expected fidelity of the quantum gate, hence providing valuable insights to strategies for choosing the optimal number of segments given a correlation strength. For a given required gate robustness, larger correlation strength implies that less segments are needed.
4. **Adiabatic and Fresnel Designs:** We introduce smooth segmented gates designs based on the principles of the Adiabatic and Fresnel scattering, that exhibit a reduced power loss while keeping the same fidelity performance. This offers a complementary tool to the traditional segmentation method.

The paper is organized as follows: In Section II, we briefly review the composite pulse design of quantum gates and the error model in the optical waveguides framework. In Section III we present the ingredients of the cost function optimization framework including the optimization range, the quantum gate fidelity and the smooth design conditions for minimizing the power loss. In Section IV we show the optimization results for the gates fidelity and power loss for a varying number of segments and for different smooth designs. Section V is devoted to a discussion and conclusions. Additional details are provided in four appendices.

II. SEGMENTED COMPOSITE PULSES

A. Robust Composite Quantum Gates

The presence of noise within the physical two-level system leads to deviations from the desired quantum gate operation. To quantify the extent to which the noisy gate deviates from the ideal gate, we define the gate fidelity F by the trace norm:

$$F(U_{\text{ideal}}, U(\epsilon)) = \frac{1}{2} \left| \text{Tr} \left(U_{\text{ideal}}^\dagger U(\epsilon) \right) \right|, \quad (1)$$

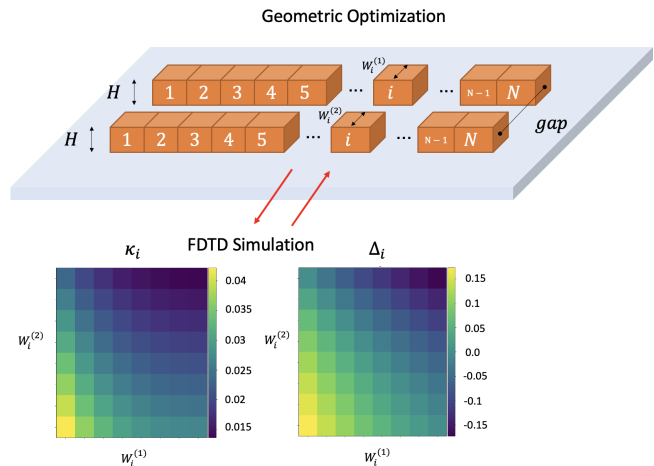


FIG. 1: We divide each of the two waveguides to N segments. Each segment i is characterized by its coupling κ_i , mode-mismatch coefficient Δ_i and length z_i . The interpolation map for κ and Δ as a function of the waveguides widths W_1, W_2 , in nm units. These results are extracted from a Lumerical FDTD Eigensolver simulation, for Silicon on insulator waveguides platform with a height of $220nm$ and a gap of $1\mu m$. One of the waveguides was illuminated with $1.55\mu m$ light source.

where U_{ideal} represents the desired ideal unitary gate, and $U(\epsilon)$ represents its physical realization, which depends on a set of m jointly distributed random errors denoted as $\epsilon = \{\epsilon^a\}_{a=1}^m$. The fidelity is a random function that takes values in the interval range $[0, 1]$, where zero and one correspond to the absence of errors and to the maximal deviation from the desired quantum gate operation, respectively. The primary objective of our analysis is to maximize the mean fidelity, denoted as $\mathbf{E}[F]$, and to minimize its standard deviation, denoted as $\sigma[F]$:

$$\begin{aligned} \mathbf{E}[F] &= \mathbb{E}_\epsilon [F(U_{\text{ideal}}, U(\epsilon))] , \\ \sigma[F] &= \sqrt{\mathbb{E}_\epsilon [F(U_{\text{ideal}}, U(\epsilon))^2] - \mathbf{E}[F]^2} . \end{aligned} \quad (2)$$

The composite pulses is a framework for error mitigation where $U(\epsilon)$ is realized as a product of N physical unitary gates:

$$U_{cp}(\vec{\epsilon}) = \prod_{i=1}^N U_i(\epsilon_i), \quad (3)$$

where $\vec{\epsilon} = (\epsilon_1, \dots, \epsilon_N)$, $\epsilon_i = \{\epsilon_i^a\}_{a=1}^m$, and U_i are constructed to achieve higher fidelity. We will consider this error mitigation scheme in the framework of dual-rail waveguides in integrated photonics.

B. Coupled Optical Waveguides

Consider the following physical photonic realization of single-qubit quantum gates, which is also the basis for constructing probabilistic two-qubit gates [23]. A coupled system of two waveguides can be described by two parameters: the coupling coefficient κ and the mode-mismatch coefficient Δ (known also as the detuning coefficient). The coupling coefficient is given by the integral over the spatial modes-overlap:

$$\kappa = \frac{c}{4\pi\lambda} \iint \left[\epsilon(x, y) - \epsilon^{(2)}(x, y) \right] \vec{E}_\perp^{(1)} \vec{E}_\perp^{(2)} dx dy, \quad (4)$$

where (1) and (2) refer to the two waveguides in the dual-rail representation, (x, y) are the transverse directions, z denotes the propagation direction and $\epsilon(x, y)$ and $\epsilon^{(2)}(x, y)$ are the permittivity distributions of the coupled waveguides system and of waveguide (2) alone, respectively. The mode-mismatch coefficient is determined by the difference between the propagation constants of the two waveguides:

$$\Delta = \frac{\beta_1 - \beta_2}{2} \equiv \frac{2\pi}{\lambda} (n_{eff_1} - n_{eff_2}), \quad (5)$$

where n_{eff_i} are the effective refraction indices in the first and second waveguides, respectively, and depend on the geometry of the waveguides. A simple solution for the propagation differential equation is constant coupling and mode-mismatch, which we refer to as one segment. It is given by (see appendix A):

$$U(\kappa, \Delta, z) = \cos(\Omega_g z) \mathbf{I} - i \frac{\kappa}{\Omega_g} \sin(\Omega_g z) \mathbf{X} + i \frac{\Delta}{\Omega_g} \sin(\Omega_g z) \mathbf{Z}, \quad (6)$$

where $\Omega_g \equiv \sqrt{\Delta^2 + \kappa^2}$, and $\mathbf{I}, \mathbf{X}, \mathbf{Z}$ are the identity matrix and Pauli matrices, respectively.

C. Segmentation

We will analyze quantum gates designs that consist of N segments (see Fig. 1). Supported by experimental evidence [24], we consider the case where in each segment, the noise affects both waveguides identically (full correlation), i.e. $\epsilon_k^{(1)} = \epsilon_k^{(2)}$, $k = 1, \dots, N$. This implies a possible significant error in the coupling coefficients κ_k , but affects less the mode-mismatch coefficients Δ_k . As to the correlation between the errors of the different segments, we will initially assume a full correlation between them, and will later relax this condition and analyze the case of a general correlation matrix. The N -segmented

gate reads:

$$U^{(N)} = \prod_{k=1}^N U(\kappa_k, \Delta_k, z_k, \epsilon_k), \quad (7)$$

where $z_k, \kappa_k, \Delta_k, \epsilon_k$ are the length of the k^{th} -segment, its coupling, its mode-mismatch coefficient and its noise, respectively.

D. Power Loss

Implementation of the composite pulse error mitigation scheme in Silicon photonics or in any other physical platform is accompanied by power loss due to back-scattering. This back-scattering is a direct consequence of the non-smooth profile of the segmented waveguide's width, and captures the total power loss (see Appendix B). The gate reflection power loss is total power transmission coefficient P_t :

$$P_t \equiv T = \prod_{k=1}^{N-1} T_k(\kappa_k, \Delta_k, z_k, \epsilon_k), \quad (8)$$

where T_k is the power transmission coefficient from the segment k to the segment $k + 1$.

Specifically, in photonics, we can estimate the back-scattering by the Fresnel equation that governs the reflection and transmission coefficients of a light transmitted between two different materials with refractive indices n_1 and n_2 (we consider the intensity):

$$R = \left(\frac{n_1 \cos \theta_i - n_2 \cos \theta_t}{n_1 \cos \theta_i + n_2 \cos \theta_t} \right)^2, \quad (9)$$

where we chose TE polarization and θ_i and θ_t are the incident and transmitted light angle, respectively. In guided propagation, the refractive index is replaced by n_{eff} , which is calculated from the overlap integral of the spatial cross-section field profile with the cross-section refractive index.

For our analysis, focusing on the TE polarization (the basic mode) and assuming small angles related to the z axis, we evaluate the total total reflection coefficient as:

$$R = 1 - T = 1 - \prod_{i=1}^{N-1} \left(1 - \left(\frac{n_{eff_{i+1}} - n_{eff_i}}{n_{eff_{i+1}} + n_{eff_i}} \right)^2 \right). \quad (10)$$

III. OPTIMIZATION FRAMEWORK

Our optimization search method is subject to several constraints. While our goal is to obtain high fidelity quantum gates, we aim to achieve it with as smooth as

possible design in order to minimize the power loss. As discussed, abrupt changes in the waveguide's width increase the power loss due to back scattering, and also give rise to higher spatial modes in the waveguide that distort the signal, hence changing the qubit state. Moreover, waveguide designs must be physically implementable subject to the manufacturing resolution.

We divide each waveguide into a sequence of N small segments, each of length z_i as shown in Fig. 1. The two waveguides are separated by a gap (defined as the distance between the centers of the waveguides) and have a height h . Our optimization uses the Lumerical FDTD results as a look-up table to inverse-map the geometry to the coupling coefficient and the mode-mismatch parameters.

A. Fidelity

We will assume that the errors in the two waveguide widths W_1 and W_2 are fully correlated and can be sampled from a Normal distribution with zero mean and a standard deviation σ , $D \sim \mathcal{N}(0, \sigma)$. For our analysis, we consider the dimensionless parameter $\sigma\% \equiv 100 \frac{\sigma}{W_{mean}}$, where

$$W_{mean} \equiv \frac{1}{2N} \sum_i (W_i^{(1)} + W_i^{(2)}) , \quad (11)$$

and we focus on the range 1% – 10%, which is approximately around $10_{nm} - 50_{nm}$. The fidelity loss term reads:

$$\mathcal{L}_F = 1 - E_{\delta W \sim D} \left[\frac{1}{2} \text{Tr} \left(U_{ideal}^\dagger U \right) \right] , \quad (12)$$

where U_{ideal} is the ideal quantum gate and U is its physical realization.

B. The Range of Width

We add a regularization in order to restrict the width of the waveguides to be in a range between the minimum and the maximum of an allowed region:

$$\mathcal{L}_\Omega = \lambda_W \sum_i \left(\max(W_i - W_{max}, 0)^2 + \min(W_{min} - W_i, 0)^2 \right) , \quad (13)$$

where λ_W is a hyperparameter for the minimal and maximal widths. We define the optimization domain $\Omega = (\Omega_{dz}, \Omega_w)$ as the set of all experimentally realizable waveguide widths. The number N of segments in the design varies between 1 and 200, and we denote by

L the total length of the design. The degrees of freedom for the optimization are the set of widths and lengths of each segment: $\{W_i^L, W_i^R, dz_i\}_{1 < i \leq N}$.

The waveguide width initialization is sampled uniformly in the range between the maximum and minimum of the feasible domain. Additionally, strong regularization is activated once the design is out of the optimization domain Ω . It is also possible to add another regularization for the total design length L , but in our analysis we do not impose this restriction. Almost all the design lengths are between $10\mu m$ and $100\mu m$.

C. Smooth Design Conditions

1. Baseline optimization

We define the baseline optimization as a search for the highest fidelity designs even with having abrupt changes between segments cross-section widths. This exhibits scattering and reflections, higher spatial modes generations and power loss, and requires a very high precision for manufacturing. Designs will be compared to the baseline ones.

2. Minimizing Fresnel Reflection

In order to reduce the power loss, we add a regularization term which reduces the back reflection coefficient. Thus, among the robust high-fidelity design parameter space, we search for the designs with the minimal power loss. The total cost function reads:

$$\mathcal{L} = \mathcal{L}_F + L_\Omega + \lambda_R R , \quad (14)$$

where $\mathcal{L}_F, L_\Omega, R$ are given by (12), (13) and (10), respectively.

3. Imposing An Adiabaticity Condition

The adiabatic theorem guarantees, under certain conditions, a smooth transition between the ground states of two different Hamiltonians [25]. In our setup we impose an adiabatic condition on the design in the form:

$$\left| \frac{\partial \beta}{\partial z} \right| \ll \beta(z) . \quad (15)$$

Assuming a power law dependence of β on the cross-section area: $\beta = aW^m$ for some a and m , where W is the width of the waveguide, we get:

$$\left| \frac{\partial W / \partial z}{W(z)} \right| \ll 1 . \quad (16)$$

We define a corresponding regularization term:

$$A = \max_i \frac{|W_{i+1} - W_i|}{\left(\frac{W_{i+1} + W_i}{2}\right) \left(\frac{z_{i+1} + z_i}{2}\right)}. \quad (17)$$

The cost function now reads:

$$\mathcal{L} = \mathcal{L}_F + L_\Omega + \lambda_A A. \quad (18)$$

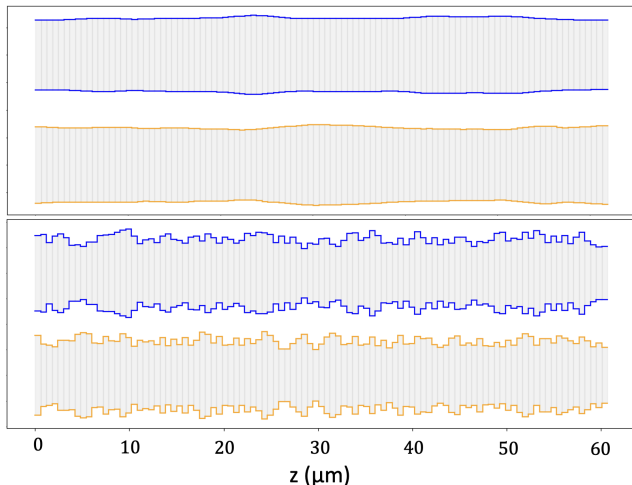


FIG. 2: Example of two 100-segments designs of \sqrt{X} gate in Silicon, with width noise standard deviation of $\sigma = 30\text{nm}$ ($\sigma\% \approx 5\%$). Top: the Fresnel-based design with expectation fidelity of 0.91 and reflection coefficient of $\pm 10^{-3}$. Bottom: the baseline with expectation fidelity of 0.9 and reflection coefficient of $\pm 10^{-2}$. The roughness standard deviation (width change along the design) is 23nm and 76nm, respectively.

D. Error Correlations

The errors at different segments may be partially correlated. In order to quantify the effect on the design performance of different strength of correlations between the errors of different segments we introduce the error correlation matrix between the $k, l \in \{1, \dots, N\}$ segments:

$$\rho_{kl}(\mu) = \begin{cases} 1 & k = l \\ \frac{1}{((k-l+1/2)^{2\mu} + 1)} & k \neq l. \end{cases} \quad (19)$$

The dimensionless parameter μ controls the strength of the correlation: $\mu = 0$ implies strong correlations between segments while $\mu \rightarrow \infty$ implies no correlation. The results of our correlations simulation will be discussed in the the simulation section (see IV C).

E. Waveguide Material

We optimize the design for two types of materials: Silicon, which is widely used in photonic applications and has a relatively high refractive index (about 3.48), and LiNbO3 which is considered to be a promising candidate for photonic applications due to its outstanding optical properties, including a wide transparency window ($0.35\mu\text{m} - 5\mu\text{m}$), large optical nonlinearity and electro-optic coefficient, and strong acousto-optic effect. The Lithium Niobate has negative uniaxial birefringence, but we assume that only the first TE_{01} mode is occupied.

For both materials we use a gap of $1.0\mu\text{m}$ and the width of each waveguide is varied between 500nm to 850nm . We further assume manufacture resolution (smallest resolution in the optimization) to be 20nm , waveguide height of 220nm , etch of 150nm and wavelength of $1.55\mu\text{m}$. To evaluate the mode-mismatch and coupling coefficients of the design we use Lumerical Eigensolver simulation (as shown in Fig. 1). We simulate different design geometries and build a look-up table to express the mode-mismatch coefficient Δ and the coupling coefficient κ in terms of the geometrical waveguide parameters. The resolution of the geometry is 5nm , and we use a bi-linear interpolation to evaluate the values in-between.

IV. OPTIMIZATION RESULTS

In the optimization we divide each waveguide into $N = 100$ segments. We use the PyTorch Package, with Adam optimizer, CosineAnnealing LR scheduler, with an initial learning rate of 0.1, batch size of 1024 samples, and the number of epochs was set to be around 5000. The device length is initialized randomly between $25\mu\text{m}$ to $100\mu\text{m}$. In our analysis we focus on the Pauli X (without mode-mismatch) and the Hadamard H (with mode-mismatch) single-qubit quantum gates. We found that other single-qubit gates show a similar behaviour. In Fig. 2 we see examples of composite designs (baseline and Fresnel based). Diagram of the trajectories on the Bloch sphere of designs for different optimization methods are shown in Fig. 3.

A. Mean Fidelity and Variance

Fig. 4 shows the expectation value and standard deviation of the fidelity for different numbers of segments taken in the range 1 to 200. To clean the optimization numerical noise, we averaged over 20 optimizations (for each number of segments). As can be clearly seen from

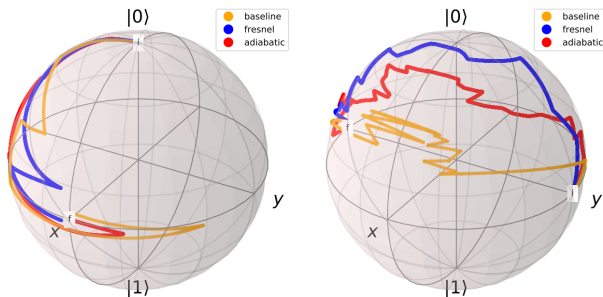


FIG. 3: Bloch Sphere diagram of two optimization results. Left - Hadamard gate with 10 segments, initial state is $|0\rangle$ and final state is $|+\rangle$. Right - Pauli X gate with 50 segments, initial state is $|+\rangle_y$ and final state is $|-\rangle_y$.

the plot, increasing the number of segments leads to an increase in the gate fidelity, and the most significant improvement is obtained when increasing the number of segments from 1 to 10. In Fig. 5 we plot the expectation value of the fidelity for different error magnitudes. Empirically, we find that the fidelity for Adiabatic and Fresnel designs are very similar to the baseline (see Fig. 9 and Appendix C for the list of the designs). We numerically observe large N scaling laws for the expectation value and variance of the fidelity as functions of the number of segments:

$$\mathbf{E}[F] \sim 1 - \frac{a}{N}, \quad \sigma[F] \sim N^{-b}, \quad (20)$$

for some constants a and b , which we expect to be non-universal and depend on the geometry of the device, the material and the wavelength. In our example, they are $a = 0.1$, and $b = 0.38$.

B. Power Loss

To evaluate the power loss of the design, we use Lumerical simulator to measure the transmitted light for each transition between two neighbouring segments with different widths. In appendix B we present a comparison between different power loss calculation methods (Fresnel coefficients, FDTD, varFDTD and EME simulations), while here we focus on the comparison between the Fresnel coefficient (up to a global factor, see appendix B for details), and the FDTD simulation result (which is considered the most accurate among the simulation methods).

Fig. 6 shows the power loss for different number of segments, for the Hadamard gate made of Lithium-Niobit material. While there are some differences between the Fresnel coefficients and the FDTD, their overall behaviour is

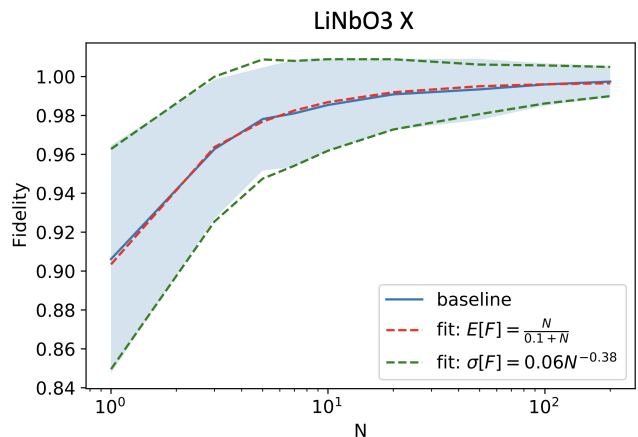


FIG. 4: Mean Fidelity and standard deviation (shaded area) versus the number of segments for Pauli X, gate and Lithium-Niobit material, assuming Normally distributed width noise with $\sigma = 30\text{nm}$ ($\sigma_{\%} \approx 5\%$). We see that the mean fidelity increases and variance decreases as the number of segments grows. This plot was created using an ensemble average over 20 optimizations for each N .

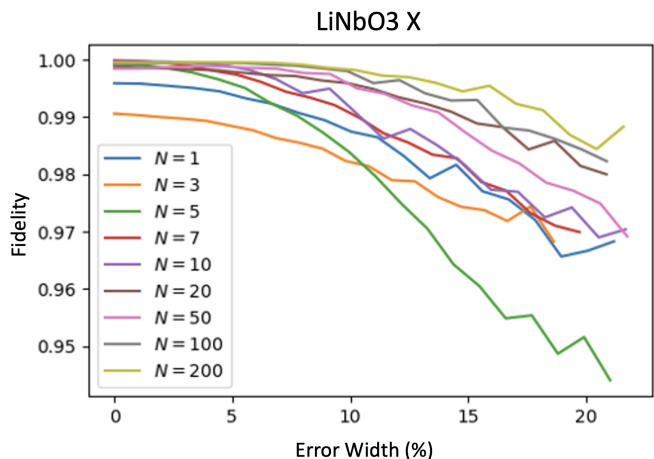


FIG. 5: The expectation value of the fidelity for different number of segments, for increasing noise width. The design is optimized for $\sigma_{\%} \approx 5\%$. Increasing the number of segments leads to a higher robustness for large width errors.

very similar. We find empirically that optimizing over the Fresnel coefficients leads to a reduction in the total power loss estimated by the FDTD. To calculate the total power loss per design, we converted the loss per transition (between segments) using Eq. 8. Fig. 6 shows the averaged result over 10 optimizations.

The averaged total power loss scaling is asymptotically linear in N :

$$\lim_{N \rightarrow \infty} \langle P_t \rangle = \lim_{N \rightarrow \infty} \left(1 - (1 - \langle R_{avg} \rangle)^{N-1} \right) = N R_{avg}, \quad (21)$$

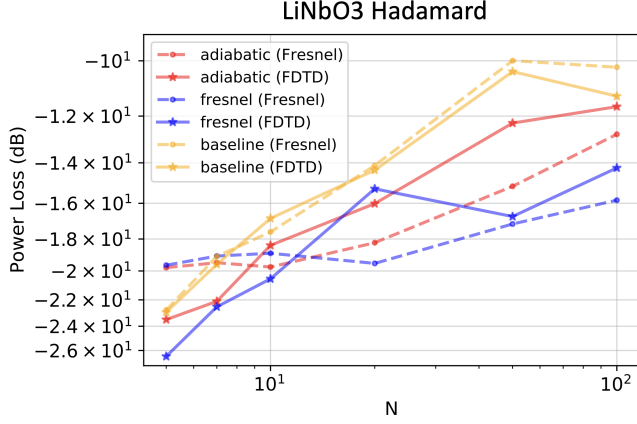


FIG. 6: Power loss versus number of segments for Hadamard, Lithium-Niobit, using Fresnel coefficients (up to a global scale factor) in dashed line and FDTD simulation in solid line. We see an increase in the power loss as the number of segments increases, with an improvement when employing the Fresnel and the Adiabatic smoothing methods. This plot is created using an ensemble average over 10 optimizations for each N and optimized for $\sigma_{\%} \approx 5\%$.

where R_{avg} is the average reflection coefficient of a transition between two adjacent segments. We plot in Fig. 7 the power density transmission cross-section curve using FDTD Lumerical simulator.

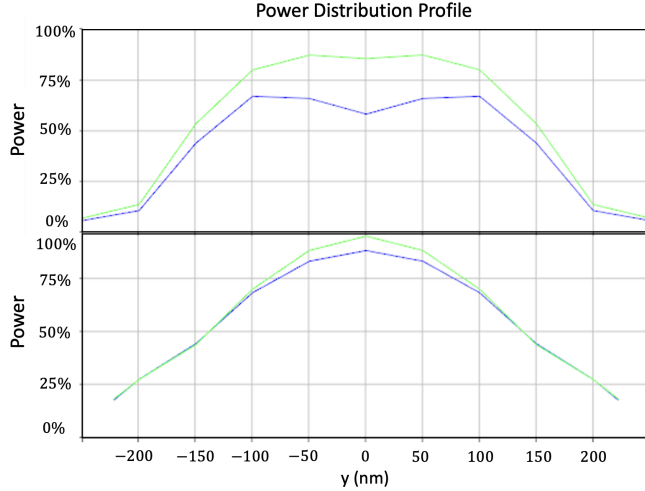


FIG. 7: Example of power density transmission cross-section curve using FDTD Lumerical simulator. The designs are of Silicon waveguides with $N = 3$: Top - Baseline, Bottom - Fresnel-based. Green - Injected light in the beginning of the waveguide, blue - transmitted light to the end of the waveguide. The horizontal axis is the spatial cross-section of the waveguide, the vertical axis is the electromagnetic wave power density profile.

C. Fidelity and Error Correlation

When the correlation between the errors at different segments decreases, the composite pulse scheme for error mitigation becomes less effective [21]. Here we analyze the impact of having a large number of segments when the error correlation decreases, where we model the error covariance matrix as (19). We plot in Fig. 8 the mean value and the standard deviation of the fidelity versus the error correlation strength μ (left, full correlation, and right, no correlation), for different numbers of segments for Pauli X gate, Silicon material. As expected, designs with a large number of segments show a better performance when the error correlations are small. We observe the same behaviour for other quantum gates.

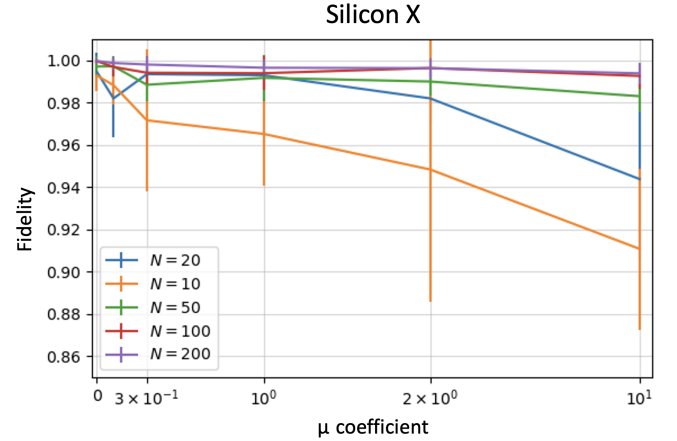


FIG. 8: Mean value and standard deviation of the fidelity versus the error correlation strength (left - full correlation and right - low correlation), for different number of segments, for gate X, Silicon. We see the improvement of the design performance when increasing the correlation and the number of segments. This plot was created using an ensemble average over 10 optimizations for each N and optimized for $\sigma_{\%} \approx 5\%$.

D. Fidelity Versus Power Loss - An Effective Error Mitigation Region

Taking into account both the fidelity of the quantum gate and the power loss of the design, we plot in Fig. 9 the mean fidelity versus the power loss and identify the effective error mitigation region. The designs are listed in table I in appendix C

V. DISCUSSION AND OUTLOOK

We studied the performance of the segmented composite pulse error mitigation scheme applied to the design of

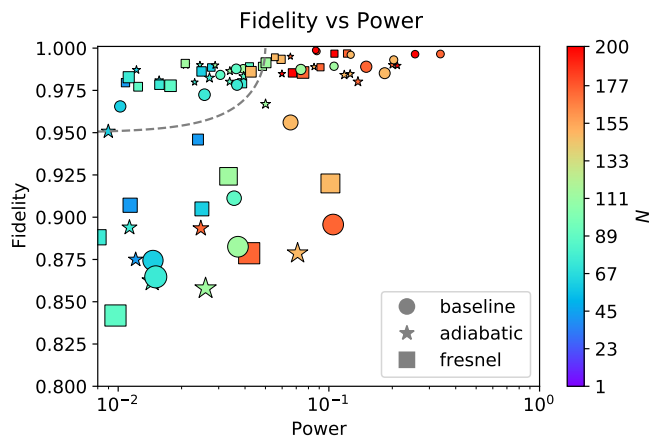


FIG. 9: Fidelity versus power loss (As calculated with the FDTD simulation). Each point represents a single design, the color indicates the number of segments N , the shape indicates the optimization type, and the size of the point indicates the fidelity's standard deviation. The dashed line defines a domain that includes designs, where the mean fidelity is very high and the power loss is very low. Table I in appendix C gives the details of the designs.

photonic quantum gates, when increasing the number of segments N and varying the error correlation strength μ . We considered the fidelity and the power loss of single-qubit quantum gates realized by optical waveguides in the dual rail framework. We quantified the impact of increasing N on the fidelity and the power loss of the quantum gates and observed certain asymptotic scaling laws. Empirically we found that $O(10)$ number of seg-

ments yields effective designs.

To reduce the power loss when increasing N , we applied two optimization regularizations by imposing constraints on the Fresnel reflection coefficient and an adiabatic condition on the waveguides width profile. We have not identified a significant difference in the gate performance between the two regularizations. However, from practical considerations it is simpler to apply the adiabatic one since it does not require a pre-calculation of the effective refraction index in the waveguide.

We studied the effect of varying the correlation strength between the errors of different segments. Large correlations between the errors imply better gate fidelity, since the different segments can effectively compensate the accumulated errors. We showed that a large number of segments allows to overcome the problem of weak error correlations.

There are several directions to follow. One is to analyze the continuum limit of the large N designs that result in smooth designs. A second one is to validate our error model against experimental data. A third direction to follow is to study the robust designs for QIP systems that include several or many quantum gates.

Acknowledgements We would like to thank J. Drori and Y. Piasetzky for their assistance in extracting parameters using Lumerical simulations. This work is supported in part by the Israeli Science Foundation Excellence Center, the US-Israel Binational Science Foundation, and the Israel Ministry of Science.

-
- [1] Charles H Bennett and David P DiVincenzo. Quantum information and computation. *nature*, 404(6775):247–255, 2000.
 - [2] C. Bennett and D. DiVincenzo. Quantum information and computation. *Nature*, 404:247–255, 2000.
 - [3] A. Montanaro. Quantum algorithms: an overview. *npj Quantum Inf*, 2(15023), 2016.
 - [4] Michael A. Nielsen and Isaac L. Chuang. *Quantum Computation and Quantum Information*. Cambridge University Press, 2000.
 - [5] Elica Kyoseva, Hadar Greener, and Haim Suchowski. Detuning-modulated composite pulses for high-fidelity robust quantum control. *Physical Review A*, 100(3):032333, 2019.
 - [6] E. Paladino, Y. M. Galperin, G. Falci, and B. L. Altshuler. $1/f$ noise: Implications for solid-state quantum information. *Rev. Mod. Phys.*, 86:361–418, Apr 2014.
 - [7] T. Grurl, C. Pichler, J. Fuß, and R. Wille. Automatic implementation and evaluation of error-correcting codes for quantum computing: An open-source framework for quantum error correction. In *2023 36th International Conference on VLSI Design and 2023 22nd International Conference on Embedded Systems (VLSID)*, pages 301–306, 2023.
 - [8] M. Urbanek, B. Nachman, V. R. Pascuzzi, A. He, C. W. Bauer, and W. A. De Jong. Mitigating depolarizing noise on quantum computers with noise-estimation circuits. *ArXiv*, 2021.
 - [9] A. Shaib, M. H. Naim, M. E. Fouda, and et al. Efficient noise mitigation technique for quantum computing. *Sci Rep*, 13:3912, 2023.
 - [10] Austin G. Fowler, Matteo Mariantoni, John M. Martinis, and Andrew N. Cleland. Surface codes: Towards practical large-scale quantum computation. *Physical Review A*, 86(3), September 2012.
 - [11] C. M. Dawson, H. L. Haselgrove, and M. A. Nielsen. Noise thresholds for optical quantum computers. *Phys. Rev. Lett.*, 96(020501):020501, 2006.
 - [12] Joschka Roffe. Quantum error correction: an introductory guide. *Contemporary Physics*, 60(3):226–245, 2019.

- [13] R. Tycko, H. M. Cho, E. Schneider, and A. Pines. Composite pulses without phase distortion. *Journal of Magnetic Resonance*, 61(1):90–101, 1985.
- [14] T. Theis, Y. Feng, T. Wu, and W. S. Warren. Composite and shaped pulses for efficient and robust pumping of disconnected eigenstates in magnetic resonance. *J Chem Phys*, 140(1):014201, 2014.
- [15] Kenneth R. Brown, Aram W. Harrow, and Isaac L. Chuang. Arbitrarily accurate composite pulse sequences. *Phys. Rev. A*, 70(052318), 2004. Erratum: *Phys. Rev. A* 72, 039905 (2005).
- [16] Alexander Dunning, Rachel Gregory, James Bateman, Nathan Cooper, Matthew Himsforth, Jonathan A. Jones, and Tim Freearge. Composite pulses for interferometry in a thermal cold atom cloud. *Phys. Rev. A*, 90(033608), 2014.
- [17] Boyan T. Torosov and Nikolay V. Vitanov. Smooth composite pulses for high-fidelity quantum information processing. *Physical Review A*, 83(5), 2011.
- [18] Sami Husain, Minaru Kawamura, and Jonathan A. Jones. Further analysis of some symmetric and antisymmetric composite pulses for tackling pulse strength errors. *Journal of Magnetic Resonance*, 230:145–154, 2013.
- [19] Ido Kaplan, Muhammad Erew, Yonatan Piasetzky, Moshe Goldstein, Yaron Oz, and Haim Suchowski. Segmented composite design of robust single-qubit quantum gates. *Physical Review A*, 108(4), October 2023.
- [20] E. Knill, R. Laflamme, and G. Milburn. A scheme for efficient quantum computation with linear optics. *Nature*, 409:46–52, 2001.
- [21] I. Kaplan, H. Suchowski, and Y. Oz. Correlation thresholds for effective composite pulse quantum error mitigation. [arXiv:2308.08691 [quant-ph]].
- [22] E. Knill, Raymond Laflamme, and Gerard J. Milburn. A scheme for efficient quantum computation with linear optics. *Nature*, 409(6816):46–52, 2001.
- [23] Amnon Yariv and Pochi Yeh. *Photonics: Optical Electronics in Modern Communications*. Oxford University Press, 6th edition, 2007.
- [24] M. Katzman and et al. Robust directional couplers for state manipulation in silicon photonic-integrated circuits. *Journal of Lightwave Technology*, 40(23):7634–7639, Dec. 1 2022.
- [25] Enrico Fermi. Method of adiabatic invariance in quantum mechanics. *Journal of the Physical Society of Japan*, 5:435–439, 1950.

Appendix A: Single Qubit Gates

The time evolution of a two-level systems (qubit) is governed by the Schrödinger equation:

$$i\partial_t \begin{pmatrix} c_1(t) \\ c_2(t) \end{pmatrix} = \begin{pmatrix} -\Delta(t) & \kappa^*(t) \\ \kappa(t) & \Delta(t) \end{pmatrix} \begin{pmatrix} c_1(t) \\ c_2(t) \end{pmatrix}, \quad (\text{A1})$$

where $c_1(t)$ and $c_2(t)$ are the probability amplitudes at time t of being in the states $|0\rangle$ and $|1\rangle$, respectively, $\kappa(t)$ is the (complex) Rabi frequency, $\Delta(t)$ is the (real) mode-mismatch, and we set $\hbar = 1$. The unitary propagator of such a system is:

$$U(t, 0) = \mathcal{T} \left[\exp \left[-i \int_0^t \begin{pmatrix} -\Delta(t') & \kappa^*(t') \\ \kappa(t') & \Delta(t') \end{pmatrix} dt' \right] \right]. \quad (\text{A2})$$

When κ and Δ are time independent, the propagator simplifies to

$$U(t, 0) = \exp \left[-it \begin{pmatrix} -\Delta & \kappa^* \\ \kappa & \Delta \end{pmatrix} \right]. \quad (\text{A3})$$

Physical systems that exhibit this $SU(2)$ dynamics implement one-qubit gates as well as probabilistic two-qubit gates. In silicon photonics, the analog of the time is the propagation axis, and the coupling coefficient κ is real. Therefore, for a single segment of length z :

$$U(\kappa, \Delta, z) = \exp[-iz(\kappa X - \Delta Z)], \quad (\text{A4})$$

where X and Z are the Pauli matrices. We can rewrite the $SU(2)$ quantum gate as:

$$U(\kappa, \Delta, z) = \exp \left[-iz\Omega_g \left(\frac{\kappa}{\Omega_g}, 0, \frac{\Delta}{\Omega_g} \right) \cdot \vec{\sigma} \right] \quad (\text{A5})$$

$$= \cos(z\Omega_g) I - \frac{\kappa}{\Omega_g} \sin(z\Omega_g) X - \frac{\Delta}{\Omega_g} \sin(z\Omega_g) Z, \quad (\text{A6})$$

where $\Omega_g \equiv \sqrt{\kappa^2 + \Delta^2}$.

Appendix B: Power Loss Simulation Comparison

In Fig. 10 we show a comparison between the power loss simulator (left) to the Fresnel coefficient (right). We consider the FDTD the most accurate simulation method and this is the reason we present this method along with the Fresnel coefficients. The Fresnel coefficient approximation of the power loss compared to the simulation, are related by a global factor of about 5 (see 6 in the main text).

Appendix C: Table of designs

In table I we present a list of designs of the Hadamard gate in Lithium Niobate and their fidelity and power loss.

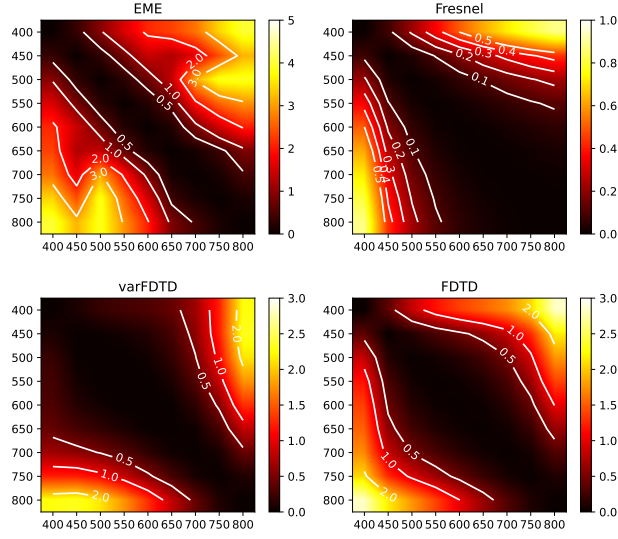


FIG. 10: Our power loss simulation using EME (top-left), Fresnel coefficients (top-right), varFDTD (bottom-left) and FDTD (bottom-right). The simulation evaluated the power loss due to a single abrupt transition from width W_1 (x axis in nm) to width W_2 (y axis in nm), for Silicon and $H = 220nm$.

TABLE I: Table of Hadamard gate designs in Lithium Niobate. Mat stands for material and PL for Power loss.

Gate	Mat	Method	E[F]	STD[F]	Length	N	PL [%]
Had	Li	adiabatic	0.8466	0.0911	29 μ m	1	0.0000
Had	Li	adiabatic	0.8990	0.0775	39 μ m	3	0.7282
Had	Li	adiabatic	0.9486	0.1012	60 μ m	5	3.0097
Had	Li	adiabatic	0.9743	0.0747	81 μ m	7	3.7159
Had	Li	adiabatic	0.9727	0.0512	77 μ m	10	4.8779
Had	Li	adiabatic	0.9237	0.0419	45 μ m	20	9.9957
Had	Li	adiabatic	0.9853	0.0250	71 μ m	50	26.0394
Had	Li	adiabatic	0.9815	0.0329	78 μ m	100	27.0626
Had	Si	adiabatic	0.8709	0.1053	47 μ m	3	2.9732
Had	Si	adiabatic	0.9173	0.1081	51 μ m	5	1.5872
Had	Si	adiabatic	0.8908	0.1171	32 μ m	7	3.0901
Had	Si	adiabatic	0.8661	0.2202	45 μ m	10	3.7749
Had	Si	adiabatic	0.8699	0.2473	34 μ m	20	5.9694
Had	Si	adiabatic	0.8941	0.2066	141 μ m	50	15.2414
Had	Si	adiabatic	0.8878	0.1263	33 μ m	100	6.3382
Had	Li	fresnel	0.8813	0.0766	35 μ m	1	0.0000
Had	Li	fresnel	0.9044	0.0866	44 μ m	3	2.1209
Had	Li	fresnel	0.9812	0.0366	71 μ m	5	6.1240
Had	Li	fresnel	0.9748	0.0618	81 μ m	7	5.8759
Had	Li	fresnel	0.9803	0.0486	72 μ m	10	3.9069
Had	Li	fresnel	0.9899	0.0359	81 μ m	20	15.5735
Had	Li	fresnel	0.9863	0.0414	59 μ m	50	11.6337
Had	Li	fresnel	0.9873	0.0441	68 μ m	100	17.4665
Had	Si	fresnel	0.8170	0.1639	27 μ m	1	0.0000
Had	Si	fresnel	0.8908	0.1565	42 μ m	3	2.7992
Had	Si	fresnel	0.9028	0.0905	48 μ m	5	4.2536
Had	Si	fresnel	0.8942	0.1031	37 μ m	7	2.2589
Had	Si	fresnel	0.7502	0.2889	44 μ m	10	6.0034
Had	Si	fresnel	0.9161	0.1656	44 μ m	20	5.9888
Had	Si	fresnel	0.9261	0.1644	130 μ m	50	20.4289
Had	Si	fresnel	0.8844	0.2194	41 μ m	100	9.6211
Had	Li	baseline	0.9623	0.0801	60 μ m	1	0.0000
Had	Li	baseline	0.9713	0.0432	88 μ m	3	3.3101
Had	Li	baseline	0.9319	0.0321	58 μ m	5	6.8709
Had	Li	baseline	0.9768	0.0447	68 μ m	7	8.9922
Had	Li	baseline	0.9854	0.0370	81 μ m	10	11.1633
Had	Li	baseline	0.9727	0.0920	68 μ m	20	19.2621
Had	Li	baseline	0.9815	0.0567	66 μ m	50	38.9191
Had	Li	baseline	0.9899	0.0489	76 μ m	100	35.6861
Had	Si	baseline	0.8779	0.1106	45 μ m	1	0.0000
Had	Si	baseline	0.8571	0.2156	30 μ m	5	2.3238
Had	Si	baseline	0.8653	0.2521	41 μ m	7	3.6235
Had	Si	baseline	0.8957	0.2226	44 μ m	10	4.4218
Had	Si	baseline	0.8750	0.2121	69 μ m	20	6.9527
Had	Si	baseline	0.9517	0.1083	150 μ m	50	12.5530
Had	Si	baseline	0.8942	0.2124	112 μ m	100	22.0704